Simulation-Ready Characterization of Soft Robotic Materials

Christian Schumacher[1], Espen Knoop[1], Moritz Bächer[1]

***Abstract*— Simulation-driven design of soft robots requires accurate and stable simulations. In this paper, we present an inverse finite element approach enabling simulation-ready characterization of soft robotic materials from uniaxial test data. Representing test specimens with finite elements, and modeling the specimen-device coupling, we enable the simultaneous fitting of hyperelastic parameters to single or multiple tests performed on specimens of varying shape and size. To safeguard against simulation instabilities, or non-physical behavior, we reparameterize and bound parameters using the consistency with linear elasticity. We use our characterization on commonly used silicones, and discuss the resolution- and order-dependence of fitted parameters, and the Mullins effect in the context of simulation-based design.**

I. Introduction

As the field of Soft Robotics matures, the complexity of the tackled problems will inevitably increase, and computational tools for simulation and optimization will become key aspects of soft robot design. However, this can only happen if soft robots can be accurately represented in simulation. Crucially, for Finite Element (FE) simulation of hyperelastic soft robots, we require a set of material parameters which accurately describe the deformation behavior of the robot. A second important consideration, in particular for optimization and inverse design problems, is that the material parameters should facilitate robust and fast simulation.

In practice, this means that we must fit *compressible* hyperelastic models to the materials. Hyperelastic models predict the complex, nonlinear behavior of soft robotic materials well, even for high-strain deformations. While most elastomers used in Soft Robotics are incompressible or nearly incompressible, enforcing incompressibility in simulations requires constraints [1], which increase time- and implementation-complexity. Hence, it is common practice to use compressible models.

Traditionally, characterization of elastomers is done by probing the uniaxial, biaxial, and potentially the triaxial material behavior, and then fitting parameters of the analytical models to data taken from uniformly deforming regions of test specimens [2].

We instead propose to represent test specimens with simulation representations, modeling their uniformly-deforming mid-regions and also their interactions at the bonding interfaces where they are pulled on. The motivation for this is threefold:

1) By also considering the non-uniformly deforming parts of specimens, we get a sufficiently rich distribution of strains to estimate high-quality parameters from a *uniaxial* displacement-force curve only. Hence, we can significantly improve prediction accuracy without the need for extensive, multi-axis testing.
2) It is well known that the stiffness, and material parameters in general, depend on the resolution and order of FEs [1]. Consequently, we can expect better performance if we *directly* estimate parameters using the representation which we later use for analysis and design.
3) Simulation performance, stability, and robustness are key factors when solving inverse design optimization tasks. To safeguard against instabilities, or mitigate problems such as locking or element inversion, it is important to account for these aspects during characterizations.

To characterize materials, we compare simulated to measured displacements, under a constraint ensuring that applied forces are in equilibrium with the elastic response of test specimens. Assigning the *same* set of material parameters to specimens used for uniaxial or biaxial testing, we enable the *unified* characterization from multi-axial data in a *single* minimization problem. To solve this equilibrium-constrained characterization, we make use of the implicit function theorem to compute analytical gradients, and couple standard FE Degrees of Freedom (DoFs) to single translational DoFs along probing directions. To warrant consistency with linear elasticity, and ensure simulation stability, we reparameterize hyperelastic parameters and bound them to prevent non-physical effects.

We demonstrate our technique on three silicones commonly used in Soft Robotics: EcoFlex™ 00-30, Smooth-Sil™ 950, and Max Mold™ 14NV. To characterize materials that exhibit the Mullins effect, we differentiate between the first- and last-pull behavior, discussing them in the context of simulation-driven design, and selection and sizing of, e.g., artificial muscles, or pneumatic actuators. We provide several validations where we study the distribution of strains in a specimen's FE representation, further motivating our approach.

II. Related Work

FE modeling is increasingly used in soft robotics work, for simulation [3, 4, 5, 6, 7], control [8, 9, 10] and for robot design optimization [11, 12].

Through open-source simulation packages such as SOFA [13] and VoxCAD [14], FE modeling tools are also accessible. However, as noted by [15], a key challenge for the adoption of such tools is that the simulation must accurately

[1]All authors are with Disney Research, Stampfenbachstrasse 48, 8006 Zurich, Switzerland. firstname.lastname@disney.com

represent the physical world, requiring parameter fitting. Our work simplifies this process for hyperelastic material models.

As well as being accurate, material parameters should also facilitate fast and robust simulations. We believe this is one bottleneck hindering the adoption of simulation and also optimization tools in soft robotics, which our method contributes to resolving.

Characterizing Hyperelastic Behavior: An extensive review is beyond the scope of this paper, and we refer the reader to the book by Odgen et al. [2] for fitting to analytical models, and to a recent survey [16] for more advanced techniques. The standard approach [17]—ubiquitous in academia and industry—is to perform uniaxial, planar tension (pure shear), and equibiaxial tests to characterize hyperelastic materials. Material parameters are then fitted using analytic models, which assume a particular deformation mode in the sample. However, multiple tests are typically required for good fits, and biaxial setups in particular are relatively complex. To remedy this, Pamplona et al. [18] propose a novel simpler membrane-based biaxial test. While we share the goal of simplifying material characterization, we aim at shifting the estimation complexity toward computation, and producing high-quality parameters from uniaxial test data only.

There have been some recent developments towards leveraging modern simulation tools for fitting hyperelastic material parameters. Connolly et al. [19] propose to use optimization to fit material parameters to the simulation representation of a single FE cube element, by applying the respective load conditions corresponding to standard material tests and solving for material parameters which best explain the data. However, they only present preliminary results. Inverse FE approaches are more common in soft tissue characterization (see, e.g., [20]). However, an equilibrium-constrained formulation enabling simultaneous characterization from multiple tests, taking resolution, order, and stability into account, is, to the best of our knowledge, novel.

Mullins effect: The softening effect of elastomers under strains was first observed by Mullins [21]. As discussed by Case et al. [22], common soft robotic materials exhibit this effect. While elastomers are commonly treated as homogeneous isotropic materials, the softening induced by prestraining a soft robot is direction-dependent, and introduces an anisotropy. Modeling and simulating this effect is involved [23], and beyond the scope of this paper. We discuss this effect, and recommend to characterize the first-pull behavior for selection of actuators, as it marks the worst-case when it comes to stiffness, and characterize prestrained specimens for applications in design.

III. Overview

As shown in Fig. 1, our uniaxial and biaxial characterization devices use linear translational stages to pull on test specimens along orthogonal axes, aligned to global coordinate axes. At all moving ends, displacements $\bar{d}$ and corresponding forces $\bar{f}$ are measured.

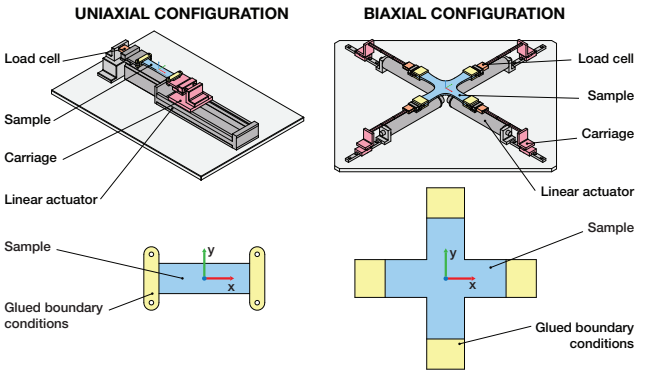

Fig. 1. **Characterization** Our uniaxial and biaxial testing devices (top) enable, together with an accurate modeling of boundary conditions (bottom), the accurate, rapid characterization of the hyperelastic behavior of common elastomers used in soft robotics.

Representing test specimens with a FE discretization (Fig. 2 right), we then seek hyperelastic material parameters that minimize differences between simulated and measured displacements, d and $\bar{d}$, by minimizing objectives of the form $\frac{1}{2}\left(d-\bar{d}\right)^2$ for every moving end, and force-displacement sample.

To improve robustness to noise, we treat the simulation forces f as parameters, and jointly optimize displacement objectives with force objectives of the form $\frac{1}{2}\left(f-\bar{f}\right)^2$, weighted by w_f.

Summing up displacement and force objectives for every moving interface k, and every sample i, we seek the parameters $\mathbf{p}$ that minimize the characterization objective

$$g_{\text{char}} = \sum_{k,i} \frac{1}{2}(d_k(\mathbf{p}, f_k^i) - \bar{d}_k^i)^2 + w_f \sum_{k,i} \frac{1}{2}(f_k^i - \bar{f}_k^i)^2. \quad (1)$$

To minimize this objective, we express standard FE DoFs that are rigidly moving with fixtures (shown in red in Fig. 3), with displacements d along global coordinate axes. We then solve the equilibrium-constrained problem

$$\begin{aligned} \min_{\mathbf{p}, f_k^i} \quad & g_{\text{char}}(\mathbf{p}, f_k^i) \\ \text{subject to} \quad & \mathbf{f}_{\text{int}}(\mathbf{p}) = \mathbf{f}_{\text{ext}}(f_k^i), \ \forall k, i \\ & \mathbf{p}_{\text{lo}} \leq \mathbf{p} \leq \mathbf{p}_{\text{up}} \end{aligned}$$

where we ask external forces $\mathbf{f}_{\text{ext}}$ to be in balance with the internal response $\mathbf{f}_{\text{int}}$ of the specimens. To keep material parameters within physically-feasible ranges, we bound them from above and below where necessary. This formulation enables the *combined* characterization from *different* tests (e.g., uniaxial and biaxial), by assigning different test specimens the *same* material parameters $\mathbf{p}$.

IV. Characterization

To efficiently solve for optimal material parameters, we require a *differentiable* simulation. We first describe how to compute analytical gradients for the single interface, single sample case, and then provide a recipe to make a standard FE implementation differentiable.

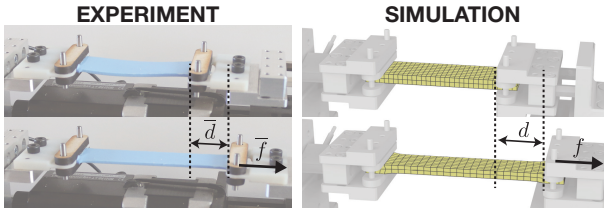

Fig. 2. **Representation**. Our uniaxial testing device (left) and its simulation representation (right).

A. Characterizing Soft Robotic Materials

As we illustrate in Fig. 2 for a single displacement-force sample $(\bar{d}, \bar{f})$, we differentiate between the FE DoFs describing the deformed configuration $\mathbf{x}$ within the test specimen, and the displacement d of bonded DoFs moving along coordinate axes. Here, $\mathbf{x}$ is a vector of size $3\times$ the number of non-interface nodes.

To discuss numerical optimization of our characterization problem, we consider the single sample case. For this case, as visualized in Fig. 2, we seek optimal parameters $\mathbf{p}$ *and* an external force f that is close to the measured force $\bar{f}$, that explain the measured displacement $\bar{d}$ with a simulated displacement d

$$g_{\text{char}}(\mathbf{y}, \mathbf{z}(\mathbf{y})) = \frac{1}{2}\left(d(\mathbf{y}) - \bar{d}\right)^2 + w_f \frac{1}{2}\left(f - \bar{f}\right)^2. \quad (2)$$

In this simplified form of our objective, we collect the *unknown* optimization variables in a vector $\mathbf{y} = (\mathbf{p}, f)$, and the elastic response of the model in a vector $\mathbf{z} = (\mathbf{x}, d)$, for conciseness.

B. Computing Analytical Derivatives

For an efficient numerical optimization, we at least need an analytical gradient. Due to the *implicit* dependence of the elastic response on the unknowns, the gradient is the total derivative

$$\mathrm{d}_{\mathbf{y}} g_{\text{char}} = \partial_{\mathbf{y}} g_{\text{char}} + \partial_{\mathbf{z}} g_{\text{char}}\, \mathrm{d}_{\mathbf{y}}\mathbf{z}. \quad (3)$$

Most entries of the two partial derivatives, $\partial_{\mathbf{y}} g_{\text{char}} = w_f(\mathbf{0}^T, f - \bar{f})$ and $\partial_{\mathbf{z}} g_{\text{char}} = (\mathbf{0}^T, d - \bar{d})$, are zero because the objective does not directly depend on the parameters $\mathbf{p}$ or the deformed DoFs $\mathbf{x}$[‡].

To compute the derivative $\mathrm{d}_{\mathbf{y}}\mathbf{z}$ of the elastic response of the specimen, we make use of the equilibrium constraint

$$\mathbf{f}(\mathbf{y}, \mathbf{z}(\mathbf{y})) = \mathbf{f}_{\text{int}}(\mathbf{p}, \mathbf{z}(\mathbf{y})) - (\mathbf{0}^T, f) = \mathbf{0}^T \quad (4)$$

that balances the nonlinear internal forces with the applied force. Because we can find an elastic response that fulfills this constraint for sets of parameters and forces in a neighborhood of a given $\mathbf{y}$, the constraint can be considered constant, and its derivative to be zero

$$\mathrm{d}_{\mathbf{y}}\mathbf{f} = \partial_{\mathbf{y}}\mathbf{f} + \partial_{\mathbf{z}}\mathbf{f}\, \mathrm{d}_{\mathbf{y}}\mathbf{z} = \mathbf{0}^T. \quad (5)$$

This application of the implicit function theorem provides us with a recipe to compute analytical gradients: Whenever we update the set of unknowns $\mathbf{y}$, we run a simulation to find the equilibrium $\mathbf{z}(\mathbf{y})$ for which the internal and external forces are in balance. We then compute the derivative of the elastic response by solving the system of equations $\mathrm{d}_{\mathbf{y}}\mathbf{z} = -\left(\partial_{\mathbf{z}}\mathbf{f}\right)^{-1}\partial_{\mathbf{y}}\mathbf{f}$, and finally evaluate Eq. 3. For the multi-interface, multi-sample case, we run simulations for *every* sample i, taking *all* forces k that act simultaneously into account.

We note that the first component of the system we have to solve, $\partial_{\mathbf{z}}\mathbf{f}$, is the tangent stiffness matrix. Further, because internal forces do not directly depend on f, we compute the partial derivative $\partial_{\mathbf{y}}\mathbf{f}$ by forming the derivative $\partial_{\mathbf{p}}\mathbf{f}_{\text{int}}$, and subtracting the derivative of the external forces with respect to f. We will expand the discussion on the first term, the derivatives of the internal forces with respect to parameters and the elastic response, in Sec. IV-D.

C. Fitting Hyperelastic Materials

We use this formulation to fit common hyperelastic material models to acquired displacement-force curves. While our technique interfaces with any model for which a strain energy density Ψ exists, we demonstrate and discuss our characterization on three representative materials that are commonly used for elastomer simulation, and are available in commercial packages: the Neo-Hookean, a generalized Mooney-Rivlin, and the 3rd-order Yeoh model.

Conditioned on having a simulator that enforces incompressibility with constraints, our method could be used to fit both *compressible* and *incompressible* models. However, FE implementations often assume a compressible model because constraint-based approaches tend to increase the time- and implementation-complexity, or can cause locking [1].

For compressible models, it is important to fit parameters that do not lead to simulation instabilities. To guarantee stability, we reparameterize materials using the consistency with linear elasticity, setting the Poisson's ratio ν to a value that is sufficiently far from 0.5. We then fit the remaining parameters.

Volume preservation terms that depend on the determinant of the deformation gradient, $J = \det \mathbf{F}$, are commonly exponentiated with an *even* number to get rid of the sign. Hence, it is important to keep corresponding parameters from taking on negative values. Negative values for parameters that weigh terms that depend on the first- or second invariants, I_1 or I_2, can lead to negative energies in moderately-deformed elements of poor quality, or highly-stretched elements of high quality. Because negative energies are non-physical, and can result in inverted elements, we bound these parameters from below, to keep them non-negative.

To demonstrate our method, we use the following compressible versions of the Neo-Hookean model

$$\Psi_{\text{NH}} = \frac{\mu}{2}\left(I_1 - 3 - 2\ln J\right) + \frac{\lambda}{2}\left(\ln J\right)^2,$$

a generalized Mooney-Rivlin model

$$\Psi_{\text{MR}} = C_{10}(\bar{I}_1 - 3) + C_{01}(\bar{I}_2 - 3) + C_{11}(\bar{I}_1 - 3)(\bar{I}_2 - 3) + D_1(J-1)^2,$$

[‡]We rely on the numerator-layout where gradients are row vectors.

TABLE I

HYPERELASTIC MATERIAL MODELS.

Ψ	sim. $\mathbf{p}$	reparam.	opt. $\mathbf{p}$
Ψ_{NH}	(μ,λ)	$\mu=\frac{E}{2(1+\nu)}$ $\lambda=\frac{E\nu}{(1+\nu)(1-2\nu)}$	$0<E<\infty$
Ψ_{MR}	$(C_{01},C_{10},C_{11},D_1)$	$D_1=\frac{2(C_{01}+C_{10})(1+\nu)}{3(1-2\nu)}$	$0<C_{01}<\infty$ $0<C_{10}<\infty$ $0<C_{11}<\infty$
Ψ_{Y}	$(C_{10},C_{20},C_{30},D_1,D_2,D_3)$	$D_1=\frac{2C_{10}(1+\nu)}{3(1-2\nu)}$	$0<C_{10}<\infty$ $0<C_{20}<\infty$ $0<C_{30}<\infty$ $0<D_2<\infty$ $0<D_3<\infty$

and the 3rd-order Yeoh model

$$\Psi_{\text{Y}} = C_{10}(\bar{I}_1-3) + C_{20}(\bar{I}_1-3)^2 + C_{30}(\bar{I}_1-3)^3 + D_1(J-1)^2 + D_2(J-1)^4 + D_3(J-1)^6.$$

The model reparameterizations, and corresponding optimization parameters with bounds, are summarized in Tab. I. If we include the Poisson's ratio in optimizations, we bound it from above and below: $0 < \nu < 0.5 - \varepsilon$ for $\varepsilon > 0$.

D. Interfacing with a Standard FE Simulation

To interface with a standard FE implementation, the coupling of a subset of DoFs to rigidly moving parts, and the differentiation of internal forces with respect to parameters, require further discussion.

While our characterization is independent of the element type and order, we favor equally-sized hexahedral elements to represent our test specimens, because: (1) numerical integration using standard Gauss quadrature is more accurate for hexahedral than for tetrahedral elements, and (2) there is no distortion in the mapping from real to natural coordinates for cubical elements. Hence, by using cubical and equally-sized hexahedral elements, we can study the resolution- and order-dependence of fitted parameters, avoiding any bias due to elements of different shape and size.

To run coupled simulations, evaluations of the internal forces $\mathbf{f}_{\text{int}}$, and the tangent stiffness $\partial_{\mathbf{z}}\mathbf{f}_{\text{int}}$ are necessary. To further discuss this, we assume familiarity with a standard energy-based implementation of a hyperelastic solid, pointing the reader to our Appendix for a brief description.

In an energy-based formulation, the internal energy $E_{\text{int}}(\overline{\mathbf{x}}, \mathbf{p})$ integrates the potential energy stored in all deformed elements. This energy depends on the nodal degrees of standard elements $\overline{\mathbf{x}}$, and the hyperelastic material parameters. To compute equilibria, we use the first and second derivative of this energy, namely the internal forces $\mathbf{f}_{\text{int}} = \partial_{\overline{\mathbf{x}}} E_{\text{int}}$ and the tangent stiffness matrix $\partial_{\overline{\mathbf{x}}}\mathbf{f}_{\text{int}}$.

To couple deformed nodes $\underline{\mathbf{x}}$ on the bonding interface to the constrained displacement d along a coordinate axis, we assume the standard DoFs to be split into non-interface and interface nodes, $\overline{\mathbf{x}} = (\mathbf{x}, \underline{\mathbf{x}})$ (Fig. 3). We then define the mapping $\overline{\mathbf{x}}(\mathbf{z}) = (\mathbf{x}, \underline{\mathbf{X}} + \boldsymbol{I}d)$ where we add the displacement

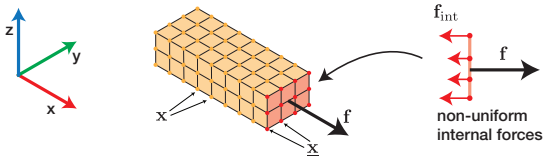

Fig. 3. **Coupling**.

d to the rest configuration $\underline{\mathbf{X}}$ of the interface nodes, with $\mathbf{I}$ set to an identity matrix of appropriate size. The derivative of this mapping, $\partial_{\mathbf{z}}\overline{\mathbf{x}}$, is the constant block diagonal matrix, $\text{diag}(\mathbf{I}, \mathbf{1})$, with identity of size of $\mathbf{x}$, and a column vector $\mathbf{1}$ with entries set to 1.

This mapping enables the evaluation of internal forces and the tangent stiffness matrix of the coupled problem with standard quantities

$$\mathbf{f}_{\text{int}} = \partial_{\overline{\mathbf{x}}} E_{\text{int}}\, \partial_{\mathbf{z}}\overline{\mathbf{x}} \quad \text{and} \quad \partial_{\mathbf{z}}\mathbf{f}_{\text{int}} = (\partial_{\mathbf{z}}\overline{\mathbf{x}})^T\, \partial_{\overline{\mathbf{x}}\overline{\mathbf{x}}} E_{\text{int}}\, \partial_{\mathbf{z}}\overline{\mathbf{x}}. \quad (6)$$

As visualized in Fig. 3, with our coupling, we correctly predict a specimen's non-uniform response that integrates to the force value f.

To compute the derivative $\partial_{\mathbf{p}}\mathbf{f}_{\text{int}}$, we assemble elemental contributions to the Jacobian $\partial_{\mathbf{p}\overline{\mathbf{x}}} E_{\text{int}}$, similarly to the assembly of the tangent stiffness matrix, and then apply the chain rule $\partial_{\mathbf{p}}\mathbf{f}_{\text{int}} = \partial_{\mathbf{p}\overline{\mathbf{x}}} E_{\text{int}}\, \partial_{\mathbf{z}}\overline{\mathbf{x}}$.

E. Optimizing for Material Parameters

Given the gradient $\mathrm{d}_{\mathbf{y}} g_{\text{char}}$ of our objective function, we can now use a quasi-Newton optimization approach with simple bound constraints to solve for material parameters. We use Knitro [24] with an L-BFGS approximation of the Hessian for this purpose. Note that the implicit inclusion of the equilibrium constraint requires that the static equilibria are recomputed whenever there is a change in design parameters, before we evaluate the objective or its derivative (Sec. IV-B). Our characterization was implemented in C++, using symbolic differentiation for derivatives with respect to elemental DoFs and to material parameters.

For a more in-depth description of a similarly-formulated optimization problem, see for example Ha et al. [25].

V. TESTING DEVICES

Our approach can readily be used with any standard material testing device (e.g. Instron) , requiring only that samples are prepared with accurately-controlled glued boundary conditions.

The uniaxial and biaxial testing devices can be seen in Fig. 1. Structural elements are machined from aluminium, for rigidity. Both devices use linear actuators (uniaxial: Zaber T-LSR-150B; biaxial: 4× Zaber T-LA60A) for displacing the samples and load cells (Futek LSB200) for force measurements. Experiments are run with a velocity of 12 mm/min.

Silicone samples are prepared by mixing and degassing the RTV silicones, then injecting them into 3d-printed molds. After curing, samples are glued to rigid interface blocks, to provide the boundary conditions. This is done in a jig, for

accuracy. Samples are glued with either Smooth-On SilPoxy or using Loctite 401 cyanoacrylate adhesive together with Loctite 770 primer. The rigid interface blocks are made from MDF, as its porosity improves adhesion.

VI. Results

We test our method on Ecoflex ™ 00-30, Mold Max™ 14NV, and Smooth-Sil™ 950 (all from Smooth-On, Inc), as they are common in soft robots, and cover a wide range of stiffnesses.

To characterize the Ecoflex™ 00-30 and Mold Max™ 14NV silicones, we use rectangular cuboidal specimens of dimensions $100 \times 25 \times 5$ mm for uniaxial testing, and unify two of these to a cross-shaped specimen for biaxial testing. For the stiffer Smooth-Sil™ 950, we use specimens of dimensions $80 \times 20 \times 2$ mm for uniaxial testing. Specimens are glued to rigidly moving parts at their two or four ends, with rectangular bonding interfaces of area 25×10 mm for softer, and area 20×10 mm for stiffer silicone on the bottom and top surfaces.

Except for the experiment studying resolution dependence, we use $40 \times 10 \times 2$ hex elements to represent longer, and $32 \times 8 \times 2$ elements to represent shorter uniaxial test specimens. For the biaxial specimen, we subtract four corners with resolutions $15 \times 15 \times 2$ from the tessellated convex hull of the specimen with $40 \times 40 \times 2$ cells, resulting in a total of $1,400$ elements. For all but our resolution and order-dependence experiments, we use quadratic elements with $n = 27$ nodes, and a 4th-order Gauss quadrature with $m = 64$ quadrature points. For all characterizations, we use a force-objective weight $w_f = 1$.

A. Fitting to Uniaxial, Biaxial, or Combined Datasets

Uniaxially and biaxially straining Ecoflex™ 00-30 specimens to a maximum strain of 125% (black curves in Fig. 4), we perform characterizations from uniaxial data, biaxial data, and a combined fit to both datasets using our technique (top row). For characterization, we rely on the Mooney-Rivlin model. Using the fitted parameters to simulate the uniaxial (top, left) or biaxial tests (top, right), we compare the fitted behavior to the experimental data.

As seen from the comparisons, we can successfully characterize the behavior from uniaxial data only. The fitted parameters predict the biaxial behavior well, and the combined fit adds marginal improvement. This result confirms one of our main motivations for this work: using a simulation representation of the *entire* test specimen enables higher quality characterizations from fewer tests.

Straining Mold Max™ 14NV specimens to 50%, we perform uniaxial, biaxial, and combined fitting (see Fig. 5). Overall, we can predict the uniaxial and biaxial behavior well. The fit to uniaxial data does not predict the biaxial behavior as well as the biaxial fit predicts the uniaxial behavior, or the combined fit predicts both behaviors.

B. Comparisons to Analytical Fitting

By tracking markers with an OptiTrack system, we extract data for the uniformly-deforming mid-regions of the EcoFlex™ 00-30 specimens. We use this data to analytically fit the material models (Fig. 4 bottom row) [2].

We observe the combined fit to predict the average uniaxial *and* biaxial behavior best. This is to be expected if only uniformly-deforming regions of specimens are considered. However, most importantly, we notice a significant error between simulations and the experimental data, clearly showing that our simulation-ready characterization outperforms analytical fitting.

C. Resolution- and Order-Dependence of Fitted Parameters

Starting with a resolution of $20 \times 5 \times 1$, we repeatedly increase the number of elements for a uniaxial test specimen, multiplying the number of cells in all directions by an increasing factor in each step. For every resolution, we run uniaxial fitting to the displacement-force curve for the Ecoflex™ 00-30 material, using linear or quadratic elements.

As we illustrate in Fig. 6 with four Mooney-Rivlin parameters, we observe a clear dependence of parameters on resolution and order of elements. While parameters converge for higher resolutions, we witness a significantly faster convergence for quadratic than for linear elements. Hence, if robots are represented with lower resolution meshes, or elements with significant differences in shape and size, we favor quadratic over linear elements (number of nodes $n = 8$) as the fitted parameter values change less over a wider range of resolutions.

D. Mullins effect

To study the Mullins effect in the context of soft robotic materials, we uniaxially strain a Smooth-Sil™ 950 specimen to 50% in a first and second pull (Fig. 7), and to 66% in a third pull. We then fit the Neo-Hookean, Mooney-Rivlin, and Yeoh models to the acquired curve. We observe that the Mooney-Rivlin and Yeoh models predict the high strain behavior better than the Neo-Hookean model.

If we worked on a soft robot where we would expect 50% strains on average, and a maximum of 66% in any direction, it is advisable to use the first pull data to determine parameters for actuator selection and sizing tasks. As the first pull marks the stiffest behavior, *independent* of the direction, we can consider this the worst-case. Hence, actuators need to be sized accordingly.

If a maximum of 66% strain is expected, the silicone cannot become softer (in any direction) than the lower bound of the curve envelope produced by repeatedly straining a sample up to 66%. Hence, for design, we could use the parameters describing the average behavior, checking the differences in performance when assigning the parameters for the softest, and for the stiffest behavior.

Note that, to account for anisotropy due to the Mullins effect, uniaxial testing and characterization is preferred as it allows us to study the isolated direction-dependence, and worst-case behavior.

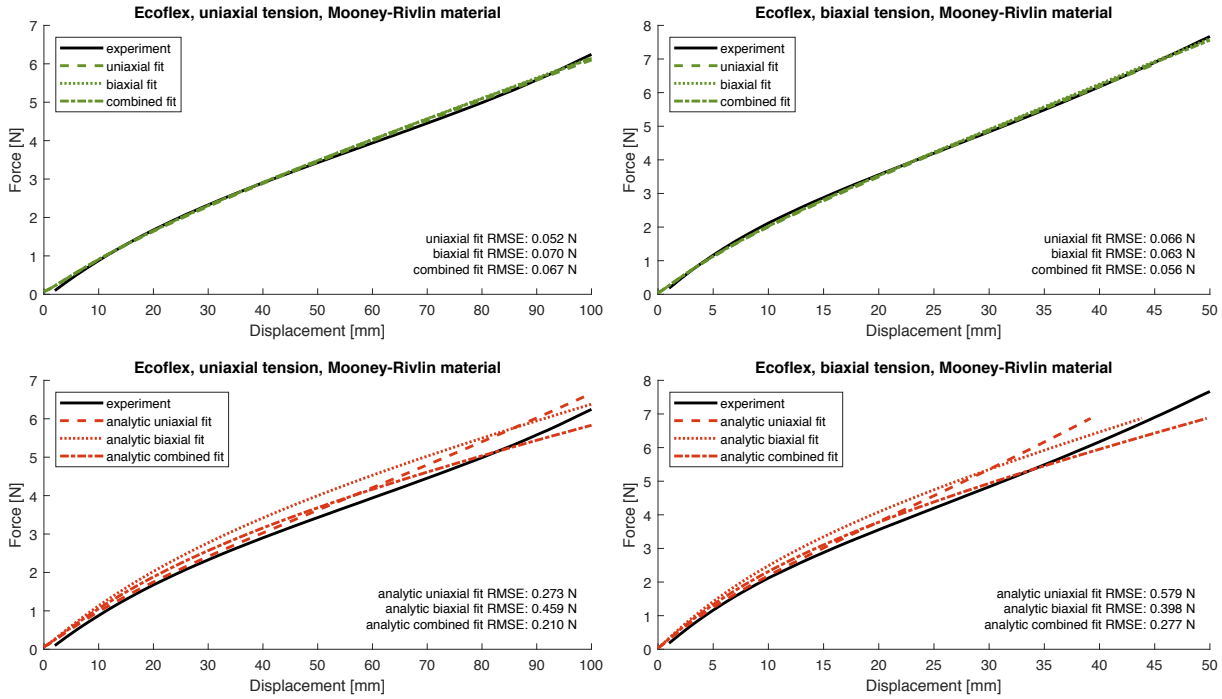

Fig. 4. **Simulation-based vs. Analytical Fitting (Ecoflex™ 00-30)** We fit to uniaxial, biaxial, and combined datasets with our simulation-based technique (top row) and traditional analytical fitting (bottom row). We then simulate the uniaxial (first column) and biaxial (second column) tests using the three sets of optimized parameters. For simulation-based fitting, uniaxial tensile data is sufficient to characterize the material while the analytical fits fail to achieve a comparable degree of prediction accuracy. For each of the fits, we have computed the Root Mean Square Error (RMSE) relative to the experimental data.

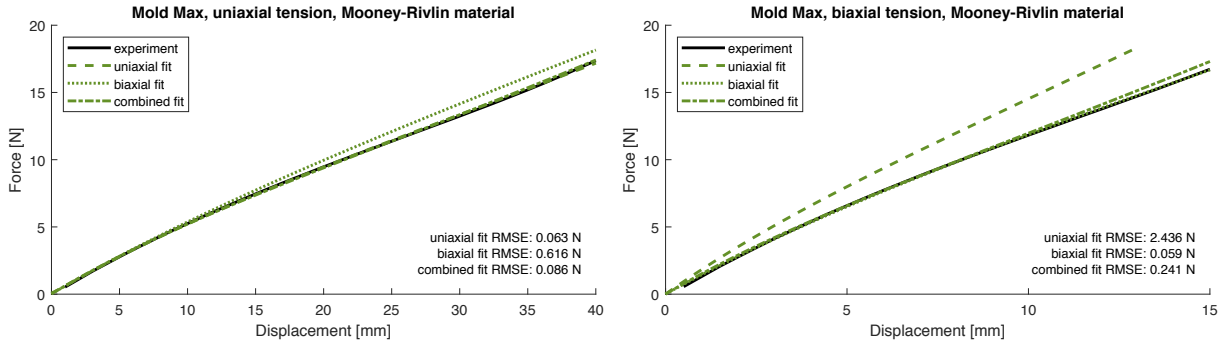

Fig. 5. **Simulation-based Fitting (Mold Max™ 14NV)** Fitting to uniaxial, biaxial, or combined datasets, we observe our combined fitting to predict the uniaxial and biaxial behavior best. Predicting the biaxial behavior with parameters fit to uniaxial data, or predicting the uniaxial behavior with parameters fit to biaxial data, we observe the biaxial fit to perform better. For each of the fits we include the RMSE relative to the experimental data.

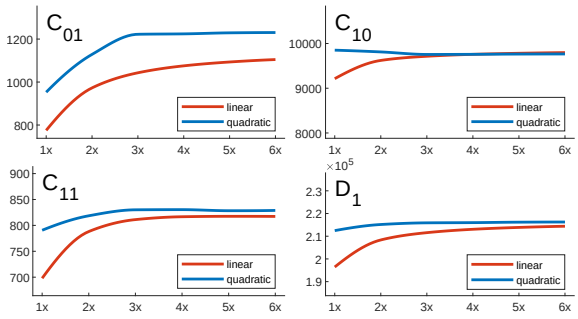

Fig. 6. **Resolution- and Order-Dependence (EcoFlex™ 00-30)** While fitted parameters (Mooney-Rivlin: $C_{01}, C_{10}, C_{11}, D_1$) converge for higher resolutions, we observe a clear dependence on resolution and order (linear vs. quadratic) of elements used for the FE representation of specimens.

E. Strain Distribution in Simulation Representations

For a 100%-strain displacement-force sample in uniaxial tension for Ecoflex™ 00-30, we plot the distribution of strains along the three global coordinate axes (Fig. 8), evaluating the deformation gradient at every quadrature point. If only the uniformly-deforming mid-region of the specimen is taken into account (as commonly done for analytical fitting), all strains in the uniaxial tension direction (x-axis) are 1 (as one would expect if we stretched a specimen to twice its length), and are compensated for with values of around -0.3 in the two orthogonal axes (due to near-incompressibility). If we additionally consider the strain distribution at the two ends, we get a rich enough distribution to enable high-quality characterizations from uniaxial test data.

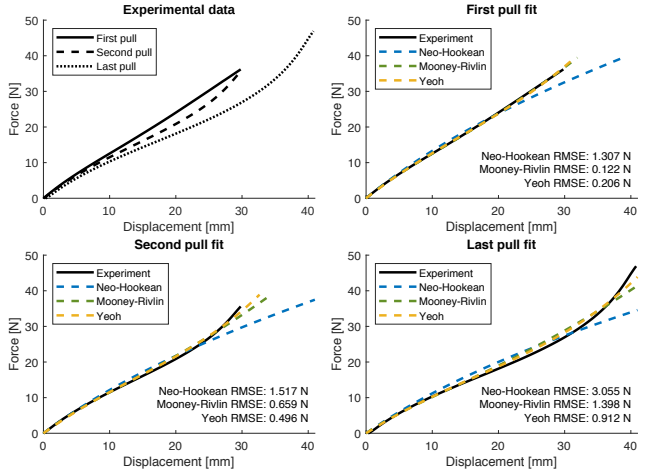

Fig. 7. **Mullins Effect (Smooth-Sil™ 950)**. Performing a first and second pull to 50%, and a third pull to 66% strain, we fit the Neo-Hookean, Mooney-Rivlin, and Yeoh materials to the three pulls, observing that the Mooney-Rivlin and Yeoh models predict the behavior better than the Neo-Hookean, especially for higher strains. For each of the fits we include the RMSE relative to the experimental data.

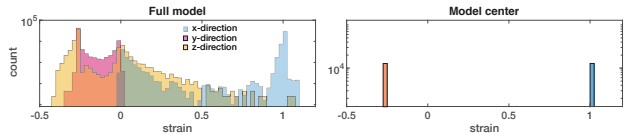

Fig. 8. **Strain Distribution (Ecoflex™ 00-30)**. Histograms (log-scale) for strains along the three global coordinate axes for a simulated uniaxial tension sample of 100%-strain (along x-direction). If we take the two ends into account (left column), the strain distribution is sufficiently rich to enable fitting from uniaxial data. If only the mid-region of specimens are considered (right column), the data is biased.

F. Sensitivity of Characterizations to Noise

In general, provided with a reasonable starting point, we observe excellent convergence to a minimum that explains the experimental data well. Assigning a set of parameters, then simulating the displacement-force curve for a uniaxial test, we started our characterization from increasingly remote starting points, successfully recovering a set that explains the simulated data well.

To understand the sensitivity of our characterization to noise in the data, we added noise of increasing variance to the forces in the Ecoflex™ 00-30 uniaxial tensile dataset. As we summarize in Fig. 9, our characterization is robust even if significant noise (stdev $\sigma = 1.249N$) is present.

G. Performance

As a representative example, on a 4.0 GHz Intel Core i7-6700K quad-core processor with 32 GB of RAM, fitting the Mooney-Rivlin material model to Ecoflex™ 00-30 took respectively 3007 s, 3250 s and 12066 s for uniaxial, biaxial, and combined test data.

VII. Conclusion

We have devised an integrated technique for simulation-ready characterization of hyperelastic materials, using a simulation representation of the *entire* test specimen to significantly improve the quality of fitted parameters from fewer mechanical tests. By shifting the estimation complexity toward computation, we show that even softer silicones under large strains can be characterized from uniaxial test data. Moreover, we discuss resolution- and order-dependence, and the Mullins effect in the context of simulation-driven design of soft robots.

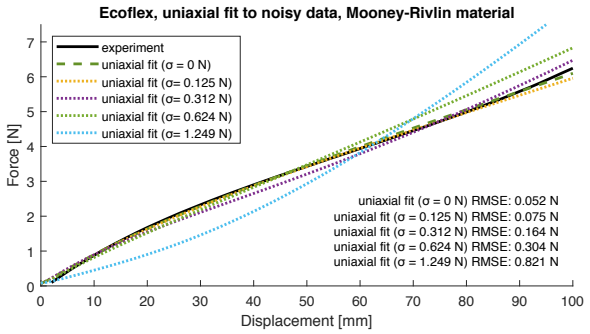

Fig. 9. **Sensitivity to Noise (Ecoflex™ 00-30)**. Even if very significant Gaussian noise is added to the forces of the Ecoflex™ 00-30) uniaxial dataset, our characterization leads to parameters that explain the data well. The RMSE behaves as would be expected, and increases gracefully.

Limitations: Our method assumes an idealized bonding of specimens to rigidly moving parts. On the hardware side, imperfections can lead to noise in the data, especially if debonding occurs. In simulations, we observe peak stresses close to boundary conditions, and, if implemented as Dirichlet conditions, stresses tend to be overestimated. Although our sensitivity study confirmed good fitting performance in the presence of noise, these issues could lead to a bias in our estimates.

Future Directions: We showed results for combined fitting to uniaxial and biaxial data. While our technique interfaces with more than these two tests, we have yet to study the difference that, e.g., a triaxial test would make. By solving for a specimen's rest configuration instead of material parameters, our computational technique could further be used to identify optimal test specimens [26, 27] that maximize strain distributions required for unbiased characterization from uniaxial, or multiaxial data.

So far, we have considered hyperelastic materials and ignored viscoelastic effects. However, our formulation could also be extended to model viscosity.

Appendix: Hyperelastic Solid Simulation

To evaluate the undeformed or deformed configuration at the natural coordinates $\boldsymbol{\xi} \in \mathbb{R}^3$ within an element, we rely on standard Lagrange shape functions $N_i(\boldsymbol{\xi})$ corresponding to element nodes i. For example, for the undeformed configuration, we interpolate the undeformed nodes $\mathbf{X}_i \in \mathbb{R}^3$

$$\mathbf{X}(\boldsymbol{\xi}) = \sum_{i=1}^{n} \mathbf{X}_i N_i(\boldsymbol{\xi}). \tag{7}$$

To measure strains within an n-node element, we define the deformation gradient as the product of the Jacobian of

the interpolated deformed nodes $\mathbf{x}_i$, and the inverse of the Jacobian $\mathbf{X}_{\boldsymbol{\xi}}$ of the undeformed configuration

$$\mathbf{F}(\boldsymbol{\xi}) = \left(\sum_{i=1}^{n} \mathbf{x}_i \partial_{\boldsymbol{\xi}} N_i(\boldsymbol{\xi}) \right) \mathbf{X}_{\boldsymbol{\xi}}^{-1}(\boldsymbol{\xi}) \tag{8}$$

where the partial derivatives $\partial_{\boldsymbol{\xi}}$ of the shape functions are, in general, not constant.

To determine the internal energy of the solid, we integrate the strain energy density Ψ over the volume $\mathcal{E}$ of the isoparametric element, taking the change of variables from real to natural coordinates into account

$$E_{\text{int}}(\overline{\mathbf{x}}, \mathbf{p}) = \sum_{e} \int_{\mathcal{E}} \Psi(\mathbf{F}(\overline{\mathbf{x}}, \boldsymbol{\xi}), \mathbf{p}) \, \det \mathbf{X}_{\boldsymbol{\xi}}(\boldsymbol{\xi}) \, \mathrm{d}\boldsymbol{\xi}. \tag{9}$$

The internal energy depends on the deformed discretized mesh nodes, collected in a vector $\overline{\mathbf{x}}$ of size $3\times$ the number of nodes, and the material parameters $\mathbf{p}$.

To evaluate the energy, we approximate the integral over $\mathcal{E}$ with an m-point Gauss quadrature

$$\sum_{j=1}^{m} w_j \Psi(\mathbf{F}(\overline{\mathbf{x}}, \boldsymbol{\xi}_j), \mathbf{p}) \, \det \mathbf{X}_{\boldsymbol{\xi}}(\boldsymbol{\xi}_j). \tag{10}$$

where w_j is the weight that corresponds to point $\boldsymbol{\xi}_j$.

To include gravity, we integrate the dot product between the gravitational vector $\mathbf{g}$ and the interpolated displacement $\mathbf{u}(\boldsymbol{\xi}) = \sum_{i=1}^{n} (\mathbf{x}_i - \mathbf{X}_i) N_i(\boldsymbol{\xi})$ over the volume enclosed by the solid

$$E_{\text{grav}}(\overline{\mathbf{x}}) = \sum_{e} \int_{\mathcal{E}} \rho \, \mathbf{g}^T \mathbf{u}(\boldsymbol{\xi}) \, \det \mathbf{X}_{\boldsymbol{\xi}}(\boldsymbol{\xi}) \, \mathrm{d}\boldsymbol{\xi}, \tag{11}$$

approximating the integral with the same quadrature scheme.

Another source of external energy is work done by nodal forces $\mathbf{f}_i \in \mathbb{R}^3$

$$E_{\text{ext}}(\overline{\mathbf{x}}) = \sum_{i} \mathbf{f}_i^T (\mathbf{x}_i - \mathbf{X}_i). \tag{12}$$

To compute the deformed configuration, we minimize the total potential energy

$$E(\overline{\mathbf{x}}) = E_{\text{int}}(\overline{\mathbf{x}}, \mathbf{p}) - E_{\text{grav}}(\overline{\mathbf{x}}) - E_{\text{ext}}(\overline{\mathbf{x}}) \tag{13}$$

to first-order optimality, $\partial_{\mathbf{x}} E = \mathbf{0}$, using a standard Newton.

References

[1] J. N. Reddy, *An introduction to nonlinear finite element analysis: with applications to heat transfer, fluid mechanics, and solid mechanics; 2nd ed.* Oxford: Oxford University Press, Jan 2015.

[2] R. W. Ogden, G. Saccomandi, and I. Sgura, "Fitting hyperelastic models to experimental data," *Computational Mechanics*, vol. 34, no. 6, pp. 484–502, 2004.

[3] K. Suzumori, S. Endo, T. Kanda, N. Kato, and H. Suzuki, "A bending pneumatic rubber actuator realizing soft-bodied manta swimming robot," in *Proc Int Conf Robotics and Automation (ICRA)*. IEEE, 2007, pp. 4975–4980.

[4] B. Mosadegh, P. Polygerinos, C. Keplinger, S. Wennstedt, R. F. Shepherd, U. Gupta, J. Shim, K. Bertoldi, C. J. Walsh, and G. M. Whitesides, "Pneumatic networks for soft robotics that actuate rapidly," *Advanced Functional Materials*, vol. 24, no. 15, pp. 2163–2170, 2014.

[5] P. Polygerinos, Z. Wang, J. T. Overvelde, K. C. Galloway, R. J. Wood, K. Bertoldi, and C. J. Walsh, "Modeling of soft fiber-reinforced bending actuators," *IEEE Trans Robotics*, vol. 31, no. 3, pp. 778–789, 2015.

[6] P. Moseley, J. M. Florez, H. A. Sonar, G. Agarwal, W. Curtin, and J. Paik, "Modeling, design, and development of soft pneumatic actuators with finite element method," *Advanced Engineering Materials*, vol. 18, no. 6, pp. 978–988, 2016.

[7] S. Y. Kim, R. Baines, J. Booth, N. Vasios, K. Bertoldi, and R. Kramer-Bottiglio, "Reconfigurable soft body trajectories using unidirectionally stretchable composite laminae," *Nature communications*, vol. 10, no. 1, p. 3464, 2019.

[8] C. Duriez, "Control of elastic soft robots based on real-time finite element method," in *Proc Int Conf Robotics and Automation (ICRA)*. IEEE, 2013, pp. 3982–3987.

[9] F. Largilliere, V. Verona, E. Coevoet, M. Sanz-Lopez, J. Dequidt, and C. Duriez, "Real-time control of soft-robots using asynchronous finite element modeling," in *Proc Int Conf Robotics and Automation (ICRA)*. IEEE, 2015, pp. 2550–2555.

[10] D. Drotman, S. Jadhav, M. Karimi, P. Dezonia, and M. T. Tolley, "3d printed soft actuators for a legged robot capable of navigating unstructured terrain," in *Proc Int Conf Robotics and Automation (ICRA)*. IEEE, 2017, pp. 5532–5538.

[11] Y. Elsayed, A. Vincensi, C. Lekakou, T. Geng, C. Saaj, T. Ranzani, M. Cianchetti, and A. Menciassi, "Finite element analysis and design optimization of a pneumatically actuating silicone module for robotic surgery applications," *Soft Robotics*, vol. 1, no. 4, pp. 255–262, 2014.

[12] J. M. Bern, K.-H. Chang, and S. Coros, "Interactive design of animated plushies," *ACM Trans Graphics (TOG)*, vol. 36, no. 4, p. 80, 2017.

[13] C. Duriez, E. Coevoet, F. Largilliere, T. Morales-Bieze, Z. Zhang, M. Sanz-Lopez, B. Carrez, D. Marchal, O. Goury, and J. Dequidt, "Framework for online simulation of soft robots with optimization-based inverse model," in *Proc Int Conf Simulation, Modeling, and Programming for Autonomous Robots (SIMPAR)*. IEEE, 2016, pp. 111–118.

[14] J. Hiller and H. Lipson, "Dynamic simulation of soft heterogeneous objects," *arXiv preprint arXiv:1212.2845*, 2012.

[15] H. Lipson, "Challenges and opportunities for design, simulation, and fabrication of soft robots," *Soft Robotics*, vol. 1, no. 1, pp. 21–27, 2014.

[16] L. A. Mihai and A. Goriely, "How to characterize a nonlinear elastic material? a review on nonlinear constitutive parameters in isotropic finite elasticity," *Proc Royal Soc A: Mathematical, Physical and Engineering Sciences*, vol. 473, no. 2207, p. 20170607, 2017.

[17] J. Gough, A. Muhr, and A. Thomas, "Material characterisation for finite element analysis of rubber components," *J Rubber Research (Malaysia)*, 1998.

[18] D. Pamplona, H. Weber, G. de Paula, and R. Velloso, "New biaxial test method for the characterization of hyperelastic rubber-like materials," in *Constitutive Models for Rubber X*. CRC Press, 08 2017, pp. 243–246.

[19] S. Connolly, D. Mackenzie, and T. Comlekci, "Multi-objective optimization of hyperelastic material constants: A feasibility study," in *10th European Conf Constitutive Models for Rubbers*, 08 2017, pp. 273–278.

[20] M. Kauer, V. Vuskovic, J. Dual, G. Szekely, and M. Bajka, "Inverse finite element characterization of soft tissues," *Medical Image Analysis*, vol. 6, no. 3, pp. 275 – 287, 2002.

[21] L. Mullins, "Effect of stretching on the properties of rubber," *Rubber Chemistry and Technology*, vol. 21, no. 2, pp. 281–300, 1948.

[22] J. C. Case, E. L. White, and R. K. Kramer, "Soft material characterization for robotic applications," *Soft Robotics*, vol. 2, no. 2, pp. 80–87, 2015.

[23] H. Wulf and J. Ihlemann, "Simulation of self-organization processes in filled rubber considering thermal agitation," 01 2012, pp. 125–130.

[24] R. H. Byrd, J. Nocedal, and R. A. Waltz, "KNITRO: An integrated package for nonlinear optimization," in *Large Scale Nonlinear Optimization*. Springer Verlag, 2006, pp. 35–59.

[25] S. Ha, S. Coros, A. Alspach, J. Kim, and K. Yamane, "Joint optimization of robot design and motion parameters using the implicit function theorem." in *Robotics: Science and Systems (RSS)*, 2017.

[26] J. Javorik and D. Manas, "The specimen optimization for the equibiaxial test of elastomers," in *Proc. 13th WSEAS Int Conf Automatic Control, Modelling & Simulation*, 05 2011, pp. 121–124.

[27] H. Seibert, T. Scheffer, and S. Diebels, "Biaxial testing of elastomers — experimental setup, measurement and experimental optimisation of specimen's shape," *Technische Mechanik*, vol. 34, pp. 72–89, 01 2014.